Chaos, Solitons and Fractals 160 (2022) 112208

Contents lists available at ScienceDirect

Chaos, Solitons and Fractals

Nonlinear Science, and Nonequilibrium and Complex Phenomena

journal homepage: www.elsevier.com/locate/chaos

Manifold dynamics and periodic orbits in a multiwell potential

H.I. Alrebdi [a], Konstantinos E. Papadakis [b], Juan F. Navarro [c,*], Euaggelos E. Zotos [d,e]

[a] Department of Physics, College of Science, Princess Nourah bint Abdulrahman University, 84428, Riyadh 11671, Saudi Arabia
[b] Department of Civil Engineering, Division of Structural Engineering, University of Patras, GR-26504 Patras, Greece
[c] Department of Applied Mathematics, University of Alicante, Carretera San Vicente del Raspeig s/n, 03690 Alicante, Spain
[d] Department of Physics, School of Science, Aristotle University of Thessaloniki, GR-541 24 Thessaloniki, Greece
[e] S.M. Nikolskii Mathematical Institute of the Peoples' Friendship University of Russia (RUDN University), Moscow 117198, Russia

ARTICLE INFO

Article history:
Received 2 February 2022
Received in revised form 2 May 2022
Accepted 8 May 2022
Available online xxxx

Keywords:
Numerical simulations
Hamiltonian systems
Invariant manifolds
Periodic orbits

ABSTRACT

In this article, we explore the dynamics as well as the geometry of the invariant manifolds that determine the escapes from a multiwell potential. We also present the network of both symmetric and asymmetric solutions of the system, while at the same time we extract valuable information about the periodic solutions, such as their locations, multiplicity, and linear stability.

1. Introduction

Multiwell potentials are of great interest in classical and quantum dynamics. One of the applications of these systems, that has focused the efforts of many research groups, is the analysis of the problem of transitions of particles from one local minimum to another, as Hamiltonian systems with multiwell potentials represent a realistic model which describes the dynamics of transition between different states of equilibrium (see e.g., [1–22]).

In fact, the main characteristic of multiwell potentials is the existence of a mixed state: for the same energy, there are different dynamical regimes in different local minima, either regular or chaotic. This means that a particle with a particular value of the energy shows a different regime of motion depending on if the particle moves in the vicinity of one local minimum or the other.

In a recent paper, Zotos [22] carries out a classification of the types of motion in a Hamiltonian system associated with the two-well umbilical catastrophe potential D_5. In his study, the author performs a numerical exploration of the system for distinguishing between bounded (ordered and chaotic) and escaping orbits, determining the basins of escape through the different openings of the potential, and also calculating the percentage of escaping orbits and its dependence on the energy of the system.

In a companion paper, Alrebdi and co-workers [1] determine how the free parameter of the two-well potential described by Zotos in [22] affects the equilibrium dynamics of the system by computing their coordinates on the configuration plane, along with their linear stability and type. Additionally, they discuss the influence of the same free parameter on the orbital dynamics of the system by performing a systematic and thorough orbit classification that reveals the bounded or escaping motion of the test particle.

The aim of this paper is, on the one hand, to clarify the geometry of the structures which determines if a particle escapes from the multiwell potential or remains trapped in the system associated with the two-well umbilical catastrophe potential D_5. On the other hand, we present the systems's families of the periodic solutions (PSs) through sets of numerical results containing the initial conditions (ICs), the time periods, as well as the stability indices of the periodic orbits inside the energetically allowed region of motion.

2. Dynamics of manifolds

In this paper, we analyze the multiwell potential

$$V_{D_5}(x,y) = 2\alpha y^2 - x^2 + xy^2 + \frac{1}{4}x^4,$$

which is the lower umbilical catastrophe D_5, in terms of the parameter $\alpha \in [-1, +1]$.

* Corresponding author.
E-mail addresses: hialrebdi@pnu.edu.sa (H.I. Alrebdi), k.papadakis@upatras.gr (K.E. Papadakis), jf.navarro@ua.es (J.F. Navarro), evzotos@physics.auth.gr (E.E. Zotos).

https://doi.org/10.1016/j.chaos.2022.112208
0960-0779/

The zero-velocity curves (ZVCs) of the system are defined by

$$2\alpha y^2 - x^2 + xy^2 + \frac{1}{4}x^4 = E,$$

where through all this analysis, α=1. These curves are represented in Fig. 1, showing in gray the regions where the motion cannot happen. When $E > E_c$, the ZVC opens, and particles may escape from the system through one of the two openings of these curves. When the ZVCs are open, there exist two unstable periodic orbits, called Lyapunov orbits (LOs), located at the openings of the potential. If a particle crosses one of these orbits pointing outwards, it escapes from the system and goes to infinity. In Fig. 1, the LOs are the almost straight lines colored in red barring the openings of the ZVCs of the system.

In the following, we analyze the geometry of the regions of fast escape of the system. To do this, we determine the ICs of the LOs located at the openings of the ZVCs of the system. Next, we calculate the stable and unstable manifolds for each of them in order to study the successive intersections of these manifolds with a suitable section surface. If the initial condition of an orbit is located inside the region enclosed by the hyper-surface defined by the stable manifold of any of the LOs, the particle will leave the potential well through the corresponding opening.

To carry out this analysis, we have fixed the value of α=1 and chosen two energy levels: E=0.1 and E=0.5. These values of the energy allow us to describe two different types of structures in the first intersections of the manifolds to the LOs with the surface of section (SoS) in which we will carry out this study. We have used the SoS defined by y=0 to study the intersections of the manifolds to the LOs.

We denote by ϕ_U to the upper LO, and by ϕ_L to the lower periodic orbit. For these orbits, we have computed the sets of the ingoing and outgoing asymptotic trajectories following the procedure described by Deprit and Henrard [23]. We denote here by $W_s(\phi)$ and $W_u(\phi)$ to the sets of ingoing and outgoing asymptotic trajectories to the LO ϕ. $W_{s,\,n}(\phi)$ denotes the n-th intersection of the stable manifold to the LO ϕ with the SoS y=0 for any $n \in$ N, and $W_{u,\,1}(\phi)$ denotes the first intersection of the unstable manifold to ϕ with the SoS y=0. Finally, we denote by $\overline{W_{s,n}(\phi)}$ and $\overline{W_{u,n}(\phi)}$ to the region delimited by the sets $W_{s,\,n}(\phi)$ and $W_{s,\,n}(\phi)$, respectively, for any $n \in$ N. Our computations unveil the following symmetry in the sets of ingoing asymptotic trajectories to ϕ_U and ϕ_L: $(x, y, \dot{y}) \in W_{s,n}(\phi_U)$ if, and only if, $(x, y, -\dot{y}) \in W_{s,n}(\phi_L)$. We have also found the same type of symmetry in the sets of outgoing asymptotic trajectories to ϕ_U and ϕ_L: $(x, y, \dot{y}) \in W_{u,n}(\phi_U)$ if, and only if, $(x, y, -\dot{y}) \in W_{u,n}(\phi_L)$. In Fig. 2, we represent a set of orbits belonging to the inner part of $W_s(\phi_U)$ and $W_u(\phi_L)$ until they intersect the SoS defined by y=0, $\dot{y} > 0$, for values of the energy given by E=0.1 (left panel) and E=0.5 (right panel).

Now, we focus on the analysis of the regions of fast escape through the upper opening of the potential. For this purpose, we calculate the three first intersections of the stable manifold to ϕ_U and the SoS y=0. The ICs belonging to $\overline{W_{s,1}(\phi_U)}$ leave the potential well through the upper opening without intersecting the SoS y=0. In general, an initial condition belonging to $\overline{W_{s,\nu}(\phi_U)}$ corresponds to an orbit that escapes from the system through the upper opening of the potential after $\nu - 1$ crossings with the SoS defined by y=0. This is the reason why we analyze the geometry of $W_{s,\,1}(\phi_U)$, $W_{s,\,2}(\phi_U)$ and $W_{s,\,3}(\phi_U)$ in order to describe the shape, size, and location of the regions of fast escape through the upper opening.

In Fig. 3, we show the first intersection of the stable manifold to ϕ_U, together with the first intersection of the unstable manifold to ϕ_L, with the SoS y=0, $\dot{y} > 0$, that is, $W_{s,\,1}(\phi_U)$ and $W_{u,\,1}(\phi_L)$, for α=1 and two values of the energy: E=0.1 (left panel) and E=0.5 (right panel). Let us stress at this point that, in both sets, $\dot{y} > 0$. We can observe that, for E=0.1, the sets $W_{s,\,1}(\phi_U)$ and $W_{u,\,1}(\phi_L)$ do not intersect. However, for E=0.5, these sets intersect and there exists a set of ICs belonging to the region delimited by both sets,

$$A_{1,1} = \overline{W_{s,1}(\phi_U)} \cap \overline{W_{u,1}(\phi_L)} \neq \emptyset.$$

The ICs belonging to $A_{1,\,1}$ correspond to orbits entering the potential through the lower opening and escaping through the upper opening, after intersecting at one point the of section y=0. We have colored in blue this set in the right panel of Fig. 3. The ICs belonging to the set $B_{1,\,1}$ are defined by

$$B_{1,1} = \overline{W_{s,1}(\phi_U)} \setminus A_{1,1}$$

have an antecedent in the SoS. Thus, we can integrate backward the ICs in $B_{1,\,1}$ to obtain the second intersection of the set of ingoing asymptotic trajectories to ϕ_U with the SoS. In order to clarify the origin of this second intersection, we have colored in green the set $B_{1,\,1}$ for the two values of the energy we have considered. We conclude that $B_{1,\,1} = W_{s,\,1}(\phi_U)$ for E=0.1 and $B_{1,\,1} \subsetneq W_{s,\,1}(\phi_U)$ for E=0.5. One of the consequences of this difference in $B_{1,\,1}$ is that $W_{s,\,2}(\phi_U)$ has a different structure for E=0.1 and E=0.5. In the following, we will analyze in detail the origin of this difference.

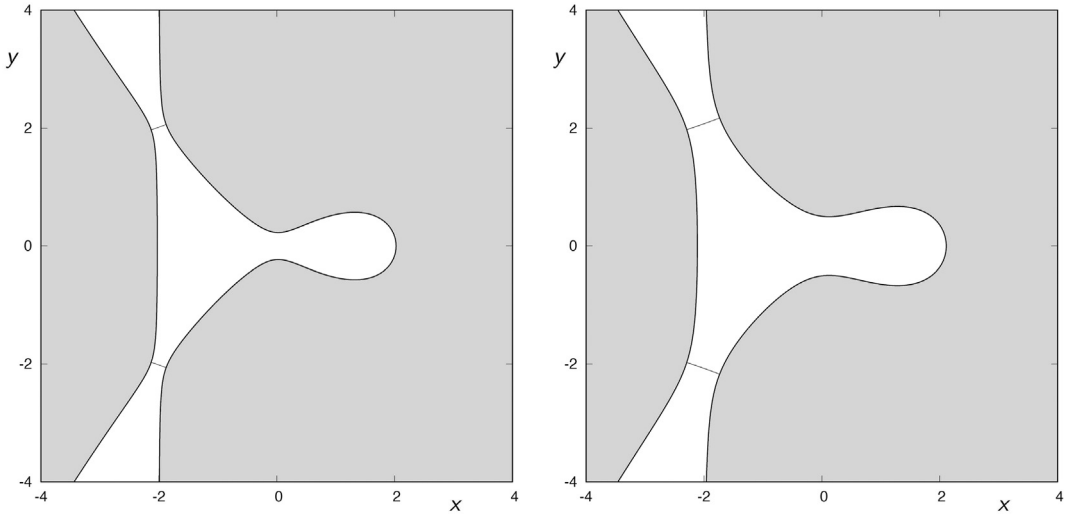

Fig. 1. ZVCs for α=1 and E=0.1 (left panel) and E=0.5 (right panel). The Lyapunov orbits ϕ_U and ϕ_L are the red and almost straight lines barring the openings of the potential. (For interpretation of the references to colour in this figure legend, the reader is referred to the web version of this article.)

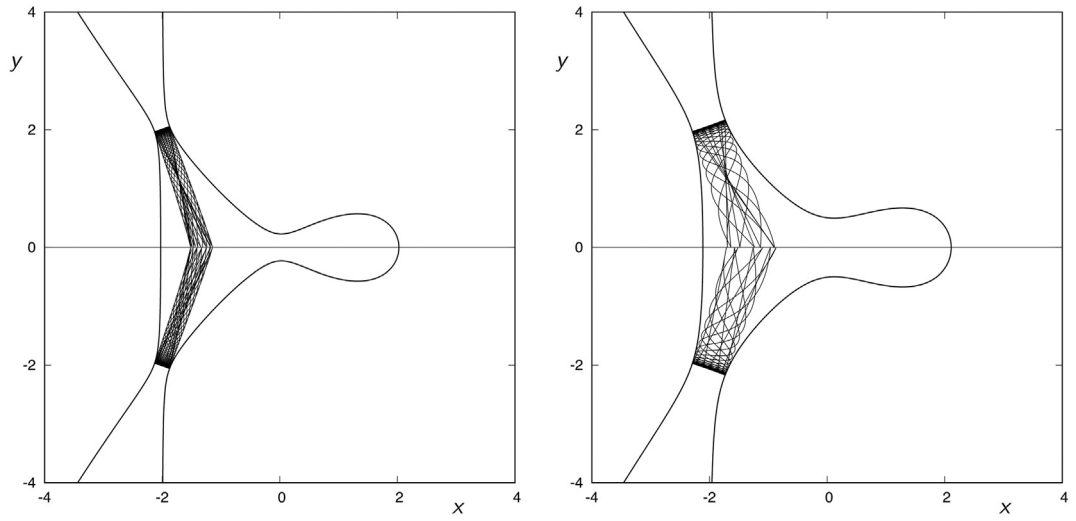

Fig. 2. Some orbits belonging to $W_s(\phi_U)$ and $W_u(\phi_L)$ for α=1 and E=0.1 (left panel) and E=0.5 (right panel).

In Fig. 4, we show the second intersection of the stable manifold to ϕ_U, together with the first intersection of the unstable manifold to ϕ_U and the first intersection of the stable manifold to ϕ_L, with the SoS defined by y=0, $\dot{y} < 0$, for α=1 and two values of the energy: E=0.1 (left panel) and E=0.5 (right panel). As done before, we must remark that the points belonging to $W_{s,\,2}(\phi_U)$, $W_{s,\,1}(\phi_L)$ and $W_{u,\,1}(\phi_U)$ have $\dot{y} < 0$. Let us define the sets

$$A_{2,1} = \overline{W_{s,2}(\phi_U)} \setminus \overline{W_{u,1}(\phi_U)}$$

and

$$B_{2,1} = \overline{W_{s,2}(\phi_U)} \setminus A_{2,1}.$$

The left panel of Fig. 4 shows that the second intersection of the set of ingoing asymptotic trajectories to ϕ_U is a simple closed curve, for E=0.1. We have colored $W_{s,\,2}(\phi_U)$ in three different tones of green: medium green for $A_{2,\,1}$ and light and dark green for the two tongue-shaped parts of $B_{2,\,1}$. The ICs in $A_{2,\,1}$, the medium green colored region, enter the potential well through the upper opening of the potential and, after intersecting two times the SoS y=0, leave the potential by the same opening, guarded by ϕ_U. The ICs in $B_{2,\,1}$ can be integrated backward in order to compute the $W_{s,\,3}(\phi_U)$.

The right panel of Fig. 4 shows that the second intersection of the set of ingoing asymptotic trajectories to ϕ_U is an infinite tongue infinitely spiraling around $W_{s,\,1}(\phi_L)$. The origin of this tongue is in the intersection between $W_{s,\,1}(\phi_U)$ and $W_{u,\,1}(\phi_L)$. The set $B_{1,\,1}$, which has a tongue shape, is transformed into an infinite tongue spiraling around $W_{s,\,1}(\phi_L)$. This infinite tongue can be decomposed into an infinite sequence of parts. Depending on the nature of these parts, we have colored them in a different tone of green. We have used medium green for the set $A_{2,\,1}$, dark green for the tip of the infinite tongue belonging to $B_{2,\,1}$, and light green for each of the bridges that connect $W_{u,\,1}(\phi_L)$ to itself. These bridges compose an infinite sequence of bridges connecting $W_{u,\,1}(\phi_L)$ with itself. The ICs in $A_{2,\,1}$ enter the potential well through the upper opening of the potential and, after intersecting two times the SoS y=0, leave the potential by the same opening, guarded by ϕ_U. The ICs in $B_{2,\,1}$ can be integrated backward in order to compute the $W_{s,\,3}(\phi_U)$.

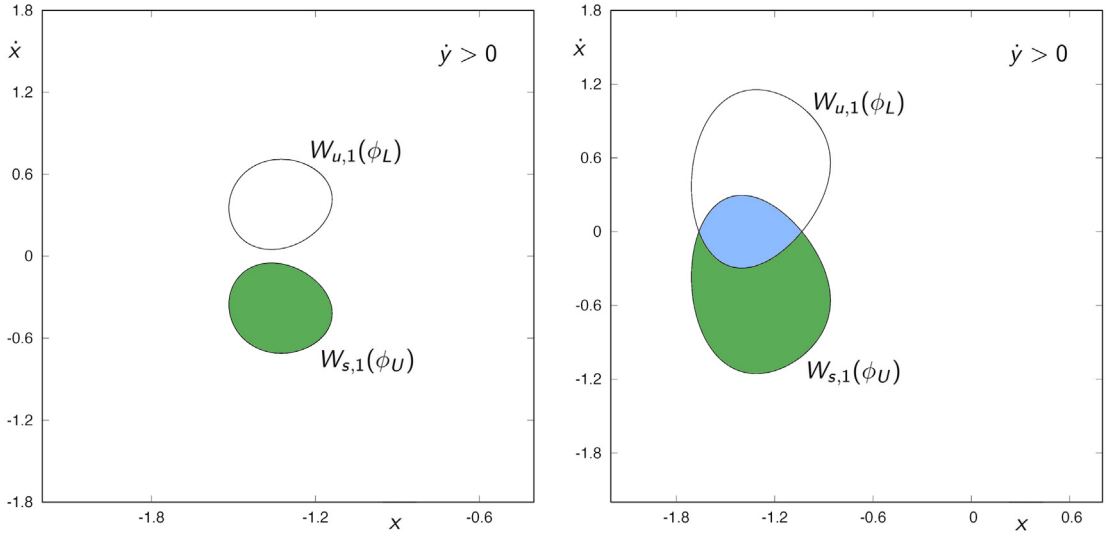

Fig. 3. $W_{s,\,1}(\phi_U)$ and $W_{u,\,1}(\phi_L)$ for α=1 and E=0.1 (left panel) and E=0.5 (right panel).

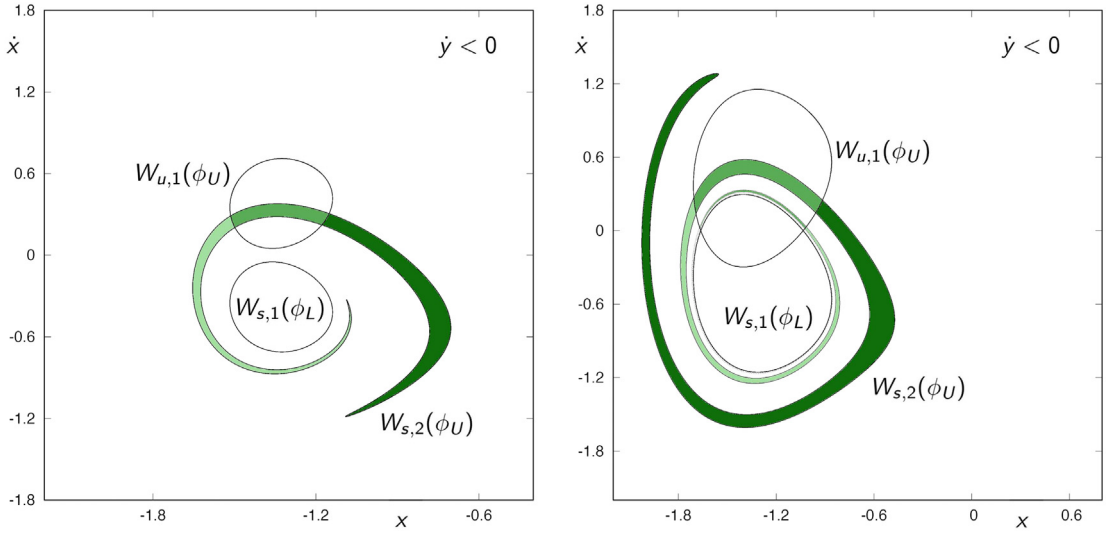

Fig. 4. $W_{s,\,2}(\phi_U)$, $W_{s,\,1}(\phi_L)$ and $W_{u,\,1}(\phi_U)$ for α=1 and E=0.1 (left panel) and E=0.5 (right panel).

Fig. 5 shows the third intersection of the stable manifold to ϕ_U, together with the first intersection of the stable manifold to ϕ_U (colored in light blue) and the second intersection of the stable manifold to ϕ_L (colored in red), with the SoS' defined by y=0, $\dot{y}$ >0, for α=1 and two values of the energy: E=0.1 (left panel) and E=0.5 (right panel). The different parts of $W_{s,\,3}(\phi_U)$ are colored in the same tone of green than its correspondent antecedent in $W_{s,\,2}(\phi_U)$.

In the left panel of Fig. 5, we show the second intersection of the set of ingoing asymptotic trajectories to ϕ_U, for E=0.1. We can observe that $W_{s,\,3}(\phi_U)$ is made up of two parts. Each of these parts has the shape of an infinite tongue spiraling around $W_{s,\,1}(\phi_U)$. We have colored each of these infinite tongues in the same colour as its antecedent in $B_{2,\,1}$ (left panel of Fig. 4). The infinite spiraling of these tongues around $W_{s,\,1}$ (ϕ_U) is due to the fact that $W_{s,\,2}(\phi_U)$ intersects $W_{u,\,1}(\phi_L)$ in the way we have described in the left panel of Fig. 4.

The structure of $W_{s,\,3}(\phi_U)$ for E=0.5 is more complicated. On the one hand, the antecedent of the dark green structure that infinitely spirals around $W_{s,\,1}(\phi_U)$ is the dark green tongue belonging to $B_{2,\,1}$. On the other hand, the infinite sequence of bridges colored in light green in the right panel of Fig. 4 is transformed in a sequence of infinite tongues spiraling around $W_{s,\,1}(\phi_U)$.

3. Periodic solutions of the system

In this section, we shall present the families of PSs of the dynamical system through sets of numerical results containing the ICs, the time periods, as well as the stability indices of the periodic orbits (POs) inside the energetically allowed region of motion. All the ICs will be presented on the (x, E)-plane, where x is the initial value of the x coordinate of the trajectory for T=0, while E is the corresponding energy level. The PSs are grouped into one-parametric families that form curves in the (x, E)-plane, known as the characteristic curves of the PSs. Without loss of the generality, all the PSs on the (x, E)-plane have a positive value of the initial velocity $\dot{y}$ >0.

3.1. Simple symmetric periodic solutions

At a first stage, we will investigate the simple symmetric (with respect to the horizontal x-axis) PSs of the system. As simple PSs, we call the simplest trajectories of the problem for which the first vertical intersection with the horizontal x-axis happens at T/2. These simple PSs are of paramount importance since they control the configuration and also the distribution of all the other (with higher multiplicity) PSs of

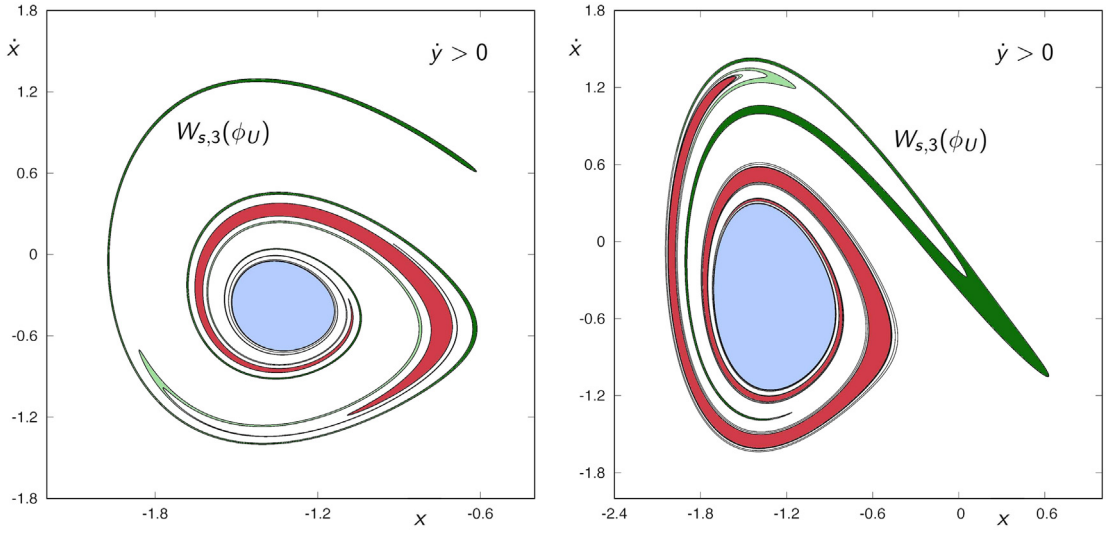

Fig. 5. $W_{s,\,3}(\phi_U)$, $W_{s,\,1}(\phi_L)$ and $W_{s,\,2}(\phi_U)$ for α=1 and E=0.1 (left panel) and E=0.5 (right panel).

the system. For this reason, we will provide an extensive analysis regarding the simple PSs of the system.

The first step for finding the simple periodic families of the system is to apply the so-called "grid-search" method [24]. According to this procedure, we approximately find the ICs of the symmetric POs, after one or more intersections with the x-axis. In our analysis, we defined a window of search in which $x \in [-4,4]$ and $E \in [-1,12]$.

The second step is to filter the approximate ICs we have already found during the first step. This is done by using a corrector-predictor convergence procedure that provides the ICs of the simple symmetric PSs with sufficient accuracy. During the numerical integration of the equations of motion as well as of the variational equations we require accuracy of at least 12 decimal digits for the ICs and at least 8 decimal digits for the periodicity of the solutions. At the same time, we also compute the horizontal linear stability for each periodic solution, using Hénon's stability indices a_h, b_h, c_h, and d_h [25,26] which are defined through the variational matrix

$$\begin{pmatrix} \Delta x \\ \Delta \dot{x} \end{pmatrix} = \begin{pmatrix} a_h & b_h \\ c_h & d_h \end{pmatrix} \begin{pmatrix} \Delta x_0 \\ \Delta \dot{x}_0 \end{pmatrix}, \tag{1}$$

where Δ_x and $\Delta \dot{x}$ are considered to maintain the energy value E, while

$$a_h = \frac{\partial x}{\partial x_0}, \; b_h = \frac{\partial x}{\partial \dot{x}_{00}}, \tag{2}$$

$$c_h = \frac{\partial \dot{x}}{\partial x_0}, d_h = \frac{\partial \dot{x}}{\partial \dot{x}_0}, \tag{3}$$

A simple periodic solution is linearly stable only if $|a_h|<1$, while if $a_h = \pm 1$ we have the case of a critical periodic solution.

Our analysis suggests that the system has nine families containing symmetric and simple POs. In Fig. 6 we present on the (x, E)-plane the characteristic curves of the nine families of simple PSs. Green and red arcs denote linearly stable and unstable solutions, respectively. The inset diagram provides a magnification of the region around the periodic families f_7, f_8, and f_9. The gray-shaded region denotes the energetically forbidden region of motion, as it is delimited by the ZVC (black curve). Moreover, small red circles pinpoint the positions of the three collinear equilibrium points L_i, i=1,2,3 of the system.

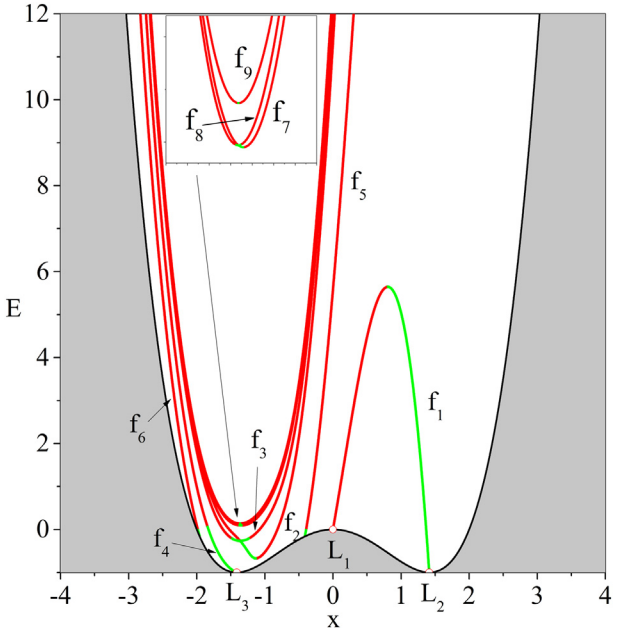

Fig. 6. The characteristic curves of the symmetric, simple periodic trajectories of the system.

The nine families of simple symmetric PSs can be categorized into two types. For the first type of symmetric orbits, at $T/2$ we have $x(T/2) = x(T=0) = x_0, y(T/2) = y_0 = 0, x(\dot{T}/2) = \dot{x}_0 = 0$, and $y(\dot{T}/2) = -\dot{y}_0$, while for the second type we have that $x(T/2) \neq x_0, y(T/2) = y_0 = 0$, $x(\dot{T}/2) = \dot{x}_0 = 0$, and $y(\dot{T}/2) \neq \dot{y}_0$. We shall call the first type of PSs "open-path" PSs (see e.g., Fig. 7a), and the second type as "closed-path" trajectories (see Fig. 7c).

The family f_1 emerges through the collinear point of equilibrium L_1 and it is composed of open-path periodic trajectories (see Fig. 7a). The corresponding characteristic curve during its time-evolution reaches a maximum energy $E \approx 5.65$ and then it reduces and finally it collides with the other point of equilibrium L_2 (see the diagram of Fig. 6). Initially (as the characteristic curve moves away from L_1), all the PSs of family f_1 are unstable, while as the characteristic curve reaches its maximum and starts heading toward L_2 the linear stability of the simple PSs changes. The corresponding diagrams with the evolution of the stability indices are given in panel (a) of Fig. 8. In all these stability diagrams, we denote the locations of critical PSs using white open circles, while white open squares indicate b_h=0. We decided to present also the parametric evolution of the stability index b_h because later on, it will help us determine the asymmetric PSs of the system.

Orbital family f_2 also contains open-path orbits (see Fig. 7b), while the corresponding characteristic curve evolves from $E_{min} \approx -0.673$, up to very high energy levels that go beyond the window of our study. The orbital family f_2 contains two branches. The right branch contains entirely unstable trajectories, while the left branch that starts from E_{min} also contains unstable solutions up to about $E = -0.265$ where it intersects with family f_3 and the stability changes. The corresponding stability diagrams are presented in panel (b) of Fig. 8.

The family f_3 is composed of closed-path trajectories (see Fig. 7c) and as we have already discussed it intersects with the orbital family f_2. The common critical periodic solution is of open-path type. The branch of f_3 at the right-hand side of the critical solution contains direct periodic trajectories (black and green orbits in Fig. 7c), while the branch at the left-hand side of the same critical orbit contains retrograde trajectories (blue orbit in Fig. 7c). According to the stability diagram of Fig. 8c, the family f_3 has only one small stability arc near the vicinity of the critical solution, which remains linearly stable up to about $E \approx -0.209$ for both branches.

The orbital family f_4 begins from the collinear point of equilibrium L_3 and contains open-path periodic trajectories (see Fig. 7d). This family is composed of only one branch that extends beyond the limit of our study (E=12). As we can see in the stability diagram of Fig. 8d, the family starts with linearly stable solutions up to the critical solution at $E \approx 0.0626$, while for higher values of the energy the stability changes. The specific critical periodic solution (red orbit in Fig. 7d) is very important. This is true because the values of the stability indices suggest that a new periodic family with asymmetric orbits bifurcates from it.

The families f_5 and f_6 have many common features since they both emerge through the ZVCs at about $E \approx -0.16$ and contain open-path trajectories (see Fig. 7e and f). The main difference is that the trajectories of family f_5 are direct, while those of family f_6 are retrograde. As one can see in Fig. 8e and f, both families start with linearly stable solutions. The stability of the orbits remains as long as the value of the total orbital energy is negative, while when E>0 the trajectories become unstable. Our conclusion is that both families f_5 and f_6 are in reality the two branches of the same family for which the respective characteristic curve has been "interrupted" by the ZVC.

Orbital family f_7 contains two branches with open-path PSs (see Fig. 7g). The inset diagram of Fig. 6 reveals that the family f_7 intersects family f_8 and that happens exactly at the position of their mutual

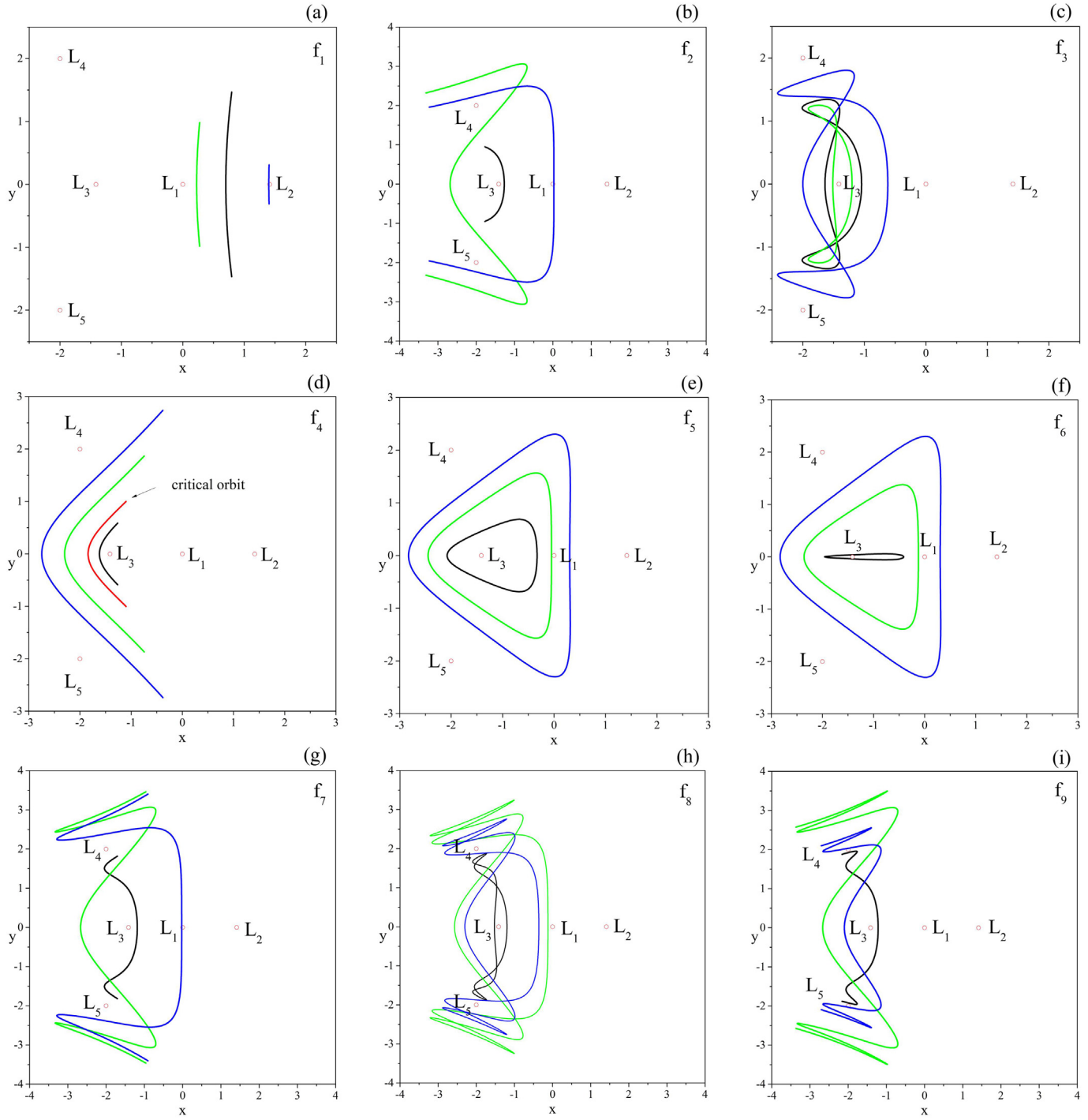

Fig. 7. Collection of all the types of symmetric, simple periodic trajectories of the system.

critical solution at $E \approx 0.097$. The periodic trajectories of the family f_7 are mainly unstable, apart from a small stability arc in the energy interval $0.095<E<0.097$.

According to the examples shown in Fig. 7h, the family f_8 contains closed-path trajectories. The characteristic curve of this family has two branches with minimum energy at $E \approx 0.0971$. The left branch contains direct trajectories (black and green orbits in Fig. 7h), while the right branch contains retrograde solutions (blue orbit in Fig. 7h). The stability diagram of Fig. 8h suggests that there is a small stability arc between $0.0971<E<0.0975$.

Finally, the orbital family f_9 is composed of open-path periodic trajectories, according to the three typical examples shown in Fig. 7i. This family has two branches and minimum energy at about $E \approx 0.137154$. The vast majority of the solutions of this family are unstable, while there is a small stability arc at the energy interval $0.137154<E<0.137174$.

The main conclusions regarding the dynamics of the symmetric, simple PSs of the system are the following:

1. The system has eight (8) families of symmetric, simple PSs since the orbital families f_5 and f_6 are in fact the two branches of the same family.

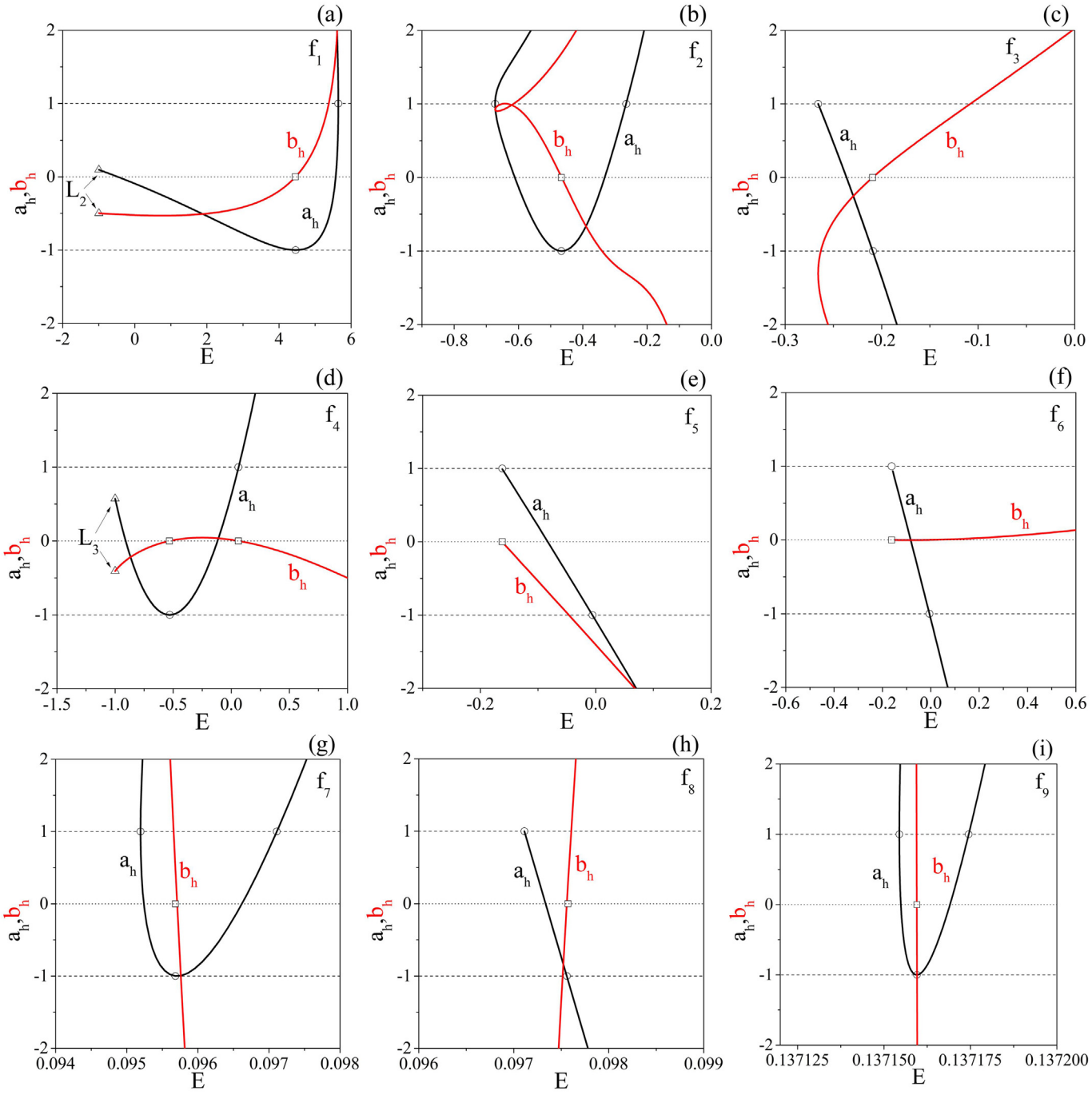

Fig. 8. Collection of the diagrams with the parametric evolution of the stability indices a_h and b_h for all families of symmetric, simple POs. White open circles and white open squares denote the positions of critical PSs for which $a_h = \pm 1$ and b_h=0, respectively.

2. The simple symmetric PSs are of two types: (i) open-path and (ii) closed-path.

3. There are five families containing open-path PSs (the families f_1, f_2, f_4, f_7, and f_9) and three families with closed-path solutions (the families f_3, $f_{5,6}$, and f_8).

4. The three families with closed-path trajectories have characteristic curves composed of two branches. For the families f_3 and f_8 the left branch contains retrograde POs and the right one direct solutions. On the other hand, for the family $f_{5,6}$ the left branch has direct solutions and the right one retrograde periodic trajectories.

5. There are four orbital families for which the corresponding characteristic curves intersect each other (f_2 with f_3 and f_7 with f_8). Always, one of these families contains open-path solutions and the other one closed-path solutions. This implies that there are no intersections with orbital families of the same type (open or closed).

6. All orbital families contain stability arcs. In most of the cases, the majority of the PSs are unstable, apart from the family f_1 for which the linearly stable arc is larger than the unstable one.

3.2. Simple asymmetric periodic solutions

In this subsection, we shall numerically investigate the existence or not of simple asymmetric PSs. By the term "asymmetric periodic solution" we refer to a trajectory with a shape that is asymmetric at least

with respect to the horizontal x-axis. The method we will use has been developed by Hénon [25–27] and it is briefly described as follows: To begin with, we choose a family of symmetric PSs and for that family, we compute the linear stability indices a_h and b_h. Then we check if a periodic solution exists with a_h=1, b_h=0, and $c_h \neq 0$, simultaneously. If so, then this specific periodic solution is a critical solution and a new family of planar asymmetric POs bifurcates from it. After finding one asymmetric periodic solution, we continue by computing the entire corresponding one-parametric family. Here, it should be noted that in the case of symmetric PSs the ICs of the trajectories are $(x_0, y_0 = 0, \dot{x}_0 = 0, \dot{y}_0(E))$, while in the case of asymmetric solutions we have $(x_0, y_0 = 0, \dot{x}_0, \dot{y}_0(E))$. This implies that asymmetric solutions have three free ICs since now the intersections with the horizontal x-axis are no longer vertical ($\dot{x}_0 \neq 0$). For the computation of the symmetric PSs the required time interval of the numerical integration of the equations of motion is equal to half of the period of the orbits, due to the symmetry of the solutions. On the other hand, in the case of asymmetric solutions, the numerical integration must be continued for the entire period of the orbits, where the conditions of periodicity are fulfilled.

For all the simple asymmetric PSs we also compute their linear horizontal stability through the index $S_h = (a_h + d_h)/2$, where a_h and d_h are the coefficients of the variational matrix. An asymmetric solution is linearly stable if $-1 < S_h < 1$ [27].

We would like to point out that in the case of symmetric PSs the presentation on the (x, E)-plane provides the full information regarding the ICs of the orbits. However, in the case of asymmetric orbits, the characteristic curves on the (x, E)-plane do not provide any kind of information regarding the horizontal and the vertical velocities of the test particle. Nevertheless, for comparison reasons (between symmetric and asymmetric PSs) we shall also use the presentation on the (x, E)-plane also for the asymmetric solutions.

Our analysis of the simple symmetric PSs suggests that only family f_4 contains a critical solution with a_h=1, b_h=0, and $c_h \neq 0$. This directly implies that only for this family we can compute the evolution of the new orbital family of asymmetric solution that bifurcates from the critical solution of f_4. Indeed, using a predictor-corrector procedure (as it is described in detail in [28]), we managed to compute the entire family of asymmetric solutions. The corresponding characteristic curve in given in Fig. 4 in blue. This family emerges through the critical solution of f_4 with ICs $x_0 = -1.84134515$, $y_0 = \dot{x}_0 = 0$, $\dot{y}_0 = 1.07635243$, $E = 0.06267596$, $T = 5.18289597$ and terminates as the coordinate x tends to zero. One of the last solutions of this asymmetric family has ICs

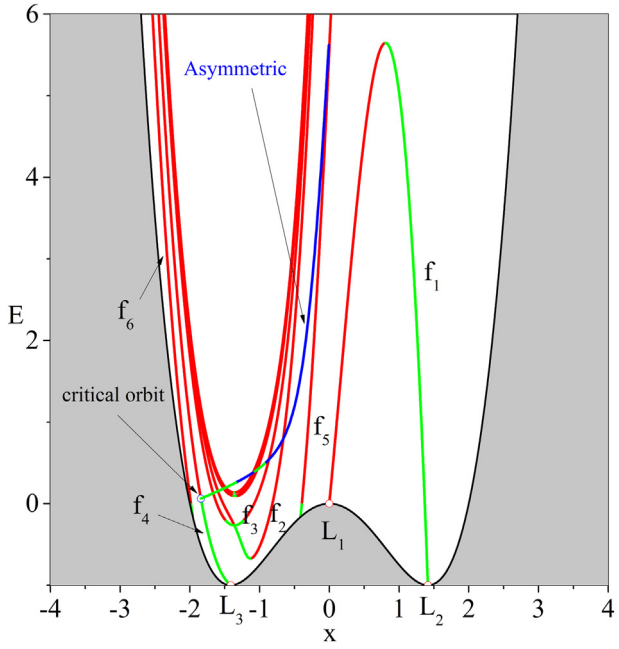

Fig. 9. The family of simple asymmetric solutions (blue curve) that bifurcates through the critical solution of the family f_4 of symmetric orbits. (For interpretation of the references to colour in this figure legend, the reader is referred to the web version of this article.)

$x_0 = -0.00163221$, $y_0 = 0$, $\dot{x}_0 = 0.62121585$, $\dot{y}_0 = 3.31729581$, $E = 5.69517764$, $T = 6.38298835$.

We computed the linear stability of all the asymmetric PSs and we found (see Fig. 10b) that this new family starts with stable solutions as it bifurcates the orbital family f_4. Then it becomes unstable, while a second stability arc appears later on. Both stability arcs of the asymmetric family are indicated in green in the corresponding characteristic curve of Fig. 9.

In the diagram of Fig. 10a, we present the characteristic curves (solid lines) of all the ICs of the family with asymmetric PSs. The same diagram contains also the characteristic curves of the symmetric family f_4 (dotted lines). The position of the critical periodic solution that acts as a bifurcation point is indicated using small, open, blue circles.

The new family is composed of open-path asymmetric PSs. Characteristic examples of asymmetric trajectories are given in Fig. 11. It is

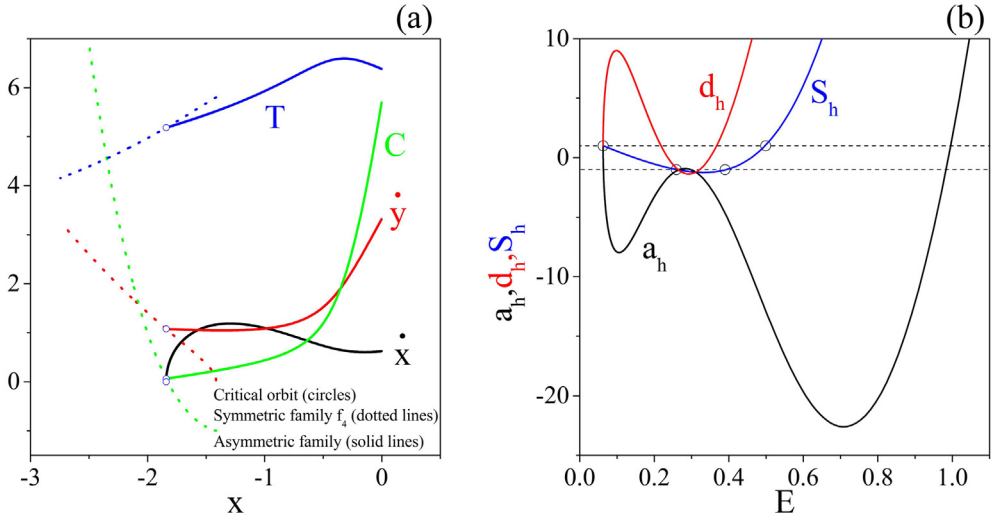

Fig. 10. (a-left): The characteristic curves of the symmetric family f_4 (dotted lines) and the asymmetric family (solid lines) that bifurcates from it. (b-right): Stability diagram of the family with asymmetric solutions.

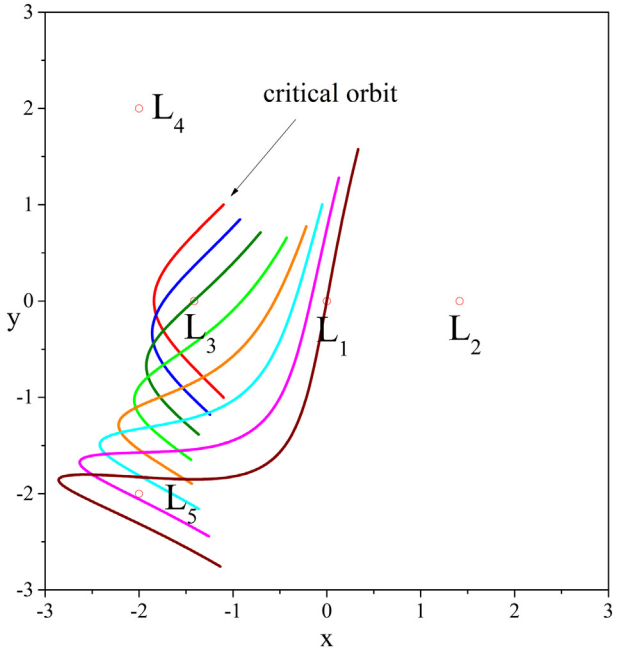

Fig. 11. Characteristic examples of simple asymmetric periodic trajectories.

seen that all the PSs are asymmetric with respect to both the horizontal x and the vertical y-axis. The starter critical periodic solution (through which the family of asymmetric solutions is born) is given in red.

3.3. Symmetric periodic solutions of higher multiplicity

In this last subsection, we investigate symmetric PSs of higher multiplicity N and in particular with $2 \le N \le 10$. A periodic solution is of multiplicity N when the first vertical intersection with the horizontal x-axis (at $T/2$) takes place after N intersections.

The first approach for computing the PSs of higher multiplicity is to use the grid-search method for obtaining approximate values of the ICs of the trajectories (note that all the solutions with $N=1$ have already been found). We restrict our search by considering only PSs with multiplicity up to 10 so as to obtain a complete view regarding the network of symmetric periodic trajectories. In Fig. 12 we present on the (x, E)-plane all the characteristic curves of symmetric POs with multiplicity up to 10. Different colors indicate trajectories with a different number of intersections with the horizontal x-axis and therefore different values of multiplicity N. The characteristic curves of simple symmetric POs (with $N=1$) are indicted with thick black curves. These simple solutions have a profound role in the configuration of all the families of higher multiplicity. In fact, simple solutions form the backbone of the network of symmetric PSs in which all the solutions of higher multiplicity bifurcate from the basic characteristic curves of the simple ($N=1$) solutions.

Indeed, as we see in the diagram of Fig. 12 the orbital families f_1 and f_4 that emerge from the equilibrium points L_2 and L_3, respectively, as well as the orbital family f_2 are the three basic families of the system. Moreover, all the characteristic curves of orbital families of higher multiplicity bifurcate from the stable arcs of these three main families of simple symmetric solutions. In Fig. 13 we provide a magnification of the area in the vicinity of the libration point L_3. Inside this region, we see that families of higher multiplicity bifurcate also from the simple orbital families f_2 and f_3. Thus, we conclude that families with symmetric PSs of higher multiplicity bifurcate from all the families of simple solutions with $N=1$.

The families of simple PSs (with $N=1$) divide the region of allowed motion into subregions where the characteristic curves of families with higher multiplicity evolve by intersecting them. For example, we see that between f_2 and f_5, f_4 and f_6, and f_3 and f_2 there exist characteristic curves of families with higher multiplicity that are trapped between the characteristic curves of the main families of multiplicity $N=1$. We also observe that the characteristic curves of the simple symmetric solutions define the boundaries of energetically allowed motion between the areas of regular and escaping motion (white regions).

In the diagram of Fig. 14 we distinguish between linearly stable (green) and unstable (red) symmetric POs of multiplicity N, with $N=1,2,...,10$. One can see, that the vast majority of the symmetric solutions are unstable, while linearly stable solutions exist mainly inside the regions of regular motion. The regions of linearly stable solutions exist near the bifurcations of the families with higher multiplicity from the

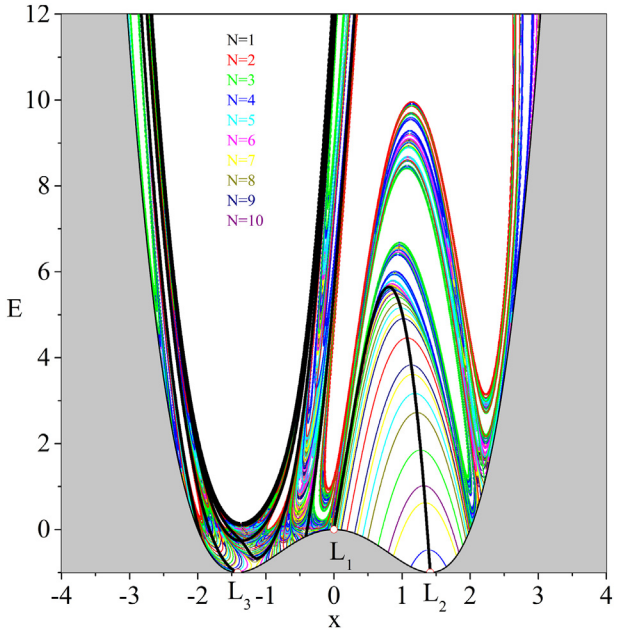

Fig. 12. Characteristic curves of symmetric POs with multiplicity $N=1,2,...,10$.

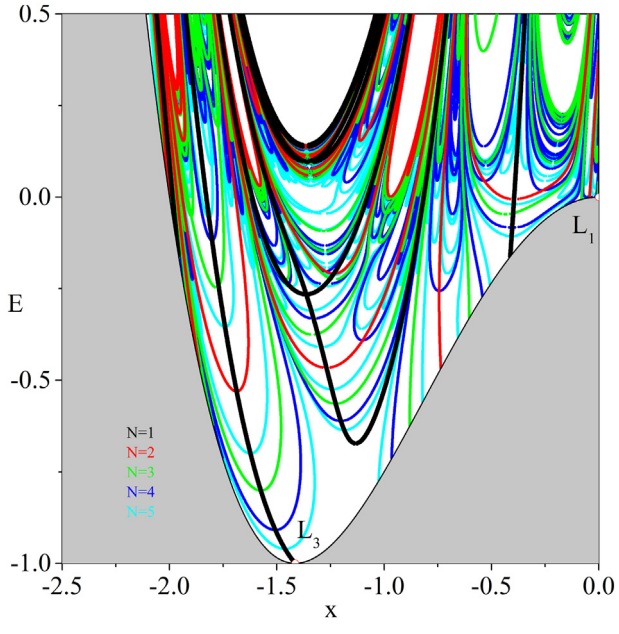

Fig. 13. Magnification of the network of symmetric POs with multiplicity up to 5, near the equilibrium point L_3.

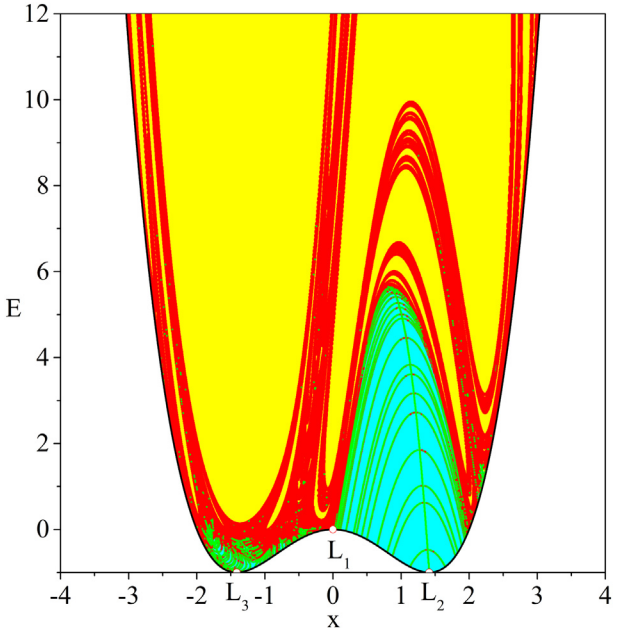

Fig. 14. The configuration of linearly stable (green) and unstable (red) symmetric POs with multiplicity N=1,2,...,10. Cyan regions correspond to regular bounded motion, while yellow regions indicate basins of escape. (For interpretation of the references to colour in this figure legend, the reader is referred to the web version of this article.)

main families with N=1 and this occurs only in the stable arcs of the characteristic curves. Furthermore, it becomes evident that linearly stable motion occurs mainly in the regions corresponding to basins of regular bounded motion (cyan areas). On the other hand, inside the basins of escape (yellow regions), there is a complete absence of any type of PSs, while ICs of unstable periodic trajectories lie inside the fractal escaping regions.

4. Discussion

This work aimed to shed some light on the dynamical properties and the geometry of the invariant manifolds of a multiwell potential. These structures have paramount importance since they control the flow (inward and outward) of particles through the several channels, associated with the system's points of equilibrium.

Apart from the manifold dynamics, we also presented in detail the network of the POs of the system, including not only symmetric but also asymmetric solutions. For these PSs, we numerically computed their locations, their multiplicity, and also their linear stability.

The results of this work along with those of [1] form a complete view regarding the orbital dynamics associated with the two-well umbilical catastrophe potential D_5.

Data availability statements

All numerical data presented in the current paper can be freely shared upon request.

Compliance with ethical standards

The authors declare that they have no conflict of interest.

Declaration of competing interest

The authors declare that they have no conflict of interest concerning the publication of this manuscript.

Acknowledgments

The present research work was funded by Princess Nourah bint Abdulrahman University Researchers Supporting Project number PNURSP2022R106, Princess Nourah bint Abdulrahman University, Riyadh, Saudi Arabia. The authors would also like to express their warmest thanks to the anonymous referees for the careful reading of the manuscript as well as for all the apt suggestions and comments which allowed us to improve both the quality and the clarity of the paper.

References

[1] H. I. Alrebdi, J. F. Navarro, E. E. Zotos, Orbital and equilibrium dynamics of a multiwell potential. Results in Physics (submitted).
[2] Aquino N, Garza J, Campoy G, Vela A. Energy eigenvalues for free and confined triple-well potentials. Rev Mex Fis. 2011;57(1):46–57.
[3] Berezovoj VP, Bolotin YuL, Ivanshkevych GI. Geometrical approach for description of the mixed state in multi-well potentials. Nonlinear Dyn Appl. 2006;13:7–13.
[4] Berezovoj VP, Bolotin YuL, Charkaskiy VA, Ivashkevych GI. Regular and Chaotic Classical and Quantum Dynamics in Multiwell Potentials. Cambridge: Cambridge Sci. Publ.; 2009.
[5] Bolotin YuL, Cherkaskiy VA, Ivashkevych GI. Decay of the mixed states. Phys Lett A. 2008;372:4080.
[6] Bolotin YuL, Cherkaskiy VA, Ivanshkevych GI, Kirdi AI. Over-barrier decay of mixed state in 2D multiwell potentials. Ukr J Phys. 2010;55(7):838–47.
[7] Cao L, Brouzos I, Zöllner S, Schmelcher P. Interaction driven interband tunneling of bosons in the triple well. New J Phys. 2011;13(3):17.
[8] Collins P, Ezra GS, Wiggins S. Index k saddles and dividing surfaces in phase space with applications to isomerization dynamics. J Chem Phys. 2011;134(24):244105.
[9] Dunne GV, Sulejmanpasic T, Ünsal M. Bions and instantons in triple-well and multi-well potentials. Roman Jackiw. 2020:119–48.
[10] Ghosh PK, Ray DS. A parametric variant of resonant activation: two-state model approach. J Chem Phys. 2006;125:124102.
[11] Kim P, Son D, Seok J. Triple-well potential with a uniform depth: advantageous aspects in designing a multi-stable energy harvester. Appl Phys Lett. 2016;108:243902.
[12] Kreibich M, Main J, Cartarius H, Wunner G. Hermitian four-well potential as a realization of a PT-symmetric system. Phys Rev A: At Mol Opt Phys. 2013;87(5):051601.
[13] Kumar P, Ruiz-Altaba M, Thomas BS. Tunneling exchange, supersymmetry, and Riccati equations. Phys Rev Lett. 1986;57:2749–51.
[14] Mahato MC, Shenoy SR. Hysteresis loss and stochastic resonance: a numerical study of a double-well potential. Phys Rev E. 1994;50(4):2503–12.
[15] Mahato MC, Jayannavar AM. Synchronized first-passages in a double-well system driven by an asymmetric periodic field. Phys Lett A. 1995;209:21–5.
[16] Mahato MC, Jayannavar AM. Some stochastic phenomena in a driven double-well system. Phys A. 1998;248:138–54.
[17] Ponzoni L, Celardo GL, Borgonovi F, Kaplan L, Kargol A. Focusing in multiwell potentials: applications to ion channels. Phys Rev E. 2013;87:052137.
[18] Selg M. Exactly solvable asymmetric double-well potentials. Phys Scr. 2016;62:108–16.
[19] Sidorov AI, Dalton BJ, Whitlock SM, Scharnberg F. Asymmetric double-well potential for single-atom interferometry. Phys Rev A. 2016;74:023612.
[20] Tian G, Zhong S-Q. A new model for the double well potential. Chin Phys Lett. 2010;27(10):100306.
[21] Zotos EE. Trapped and escaping orbits in an axially symmetric galactic-type potential. PASA. 2012;29:161–73.
[22] Zotos EE. Fractal basin boundaries and escape dynamics in a multiwell potential. Nonlinear Dyn. 2016;85:1613–33.
[23] Deprit A, J.. Henrard J construction of orbits asymptotic to a periodic orbit. Astron J. 1969;74:308–16.
[24] Markellos VV, Black W, Moran PE. A grid search for families of periodic orbits in the restricted problem of three bodies. Celes Mech. 1974;9:507–12.
[25] Hénon M. Exploration Numérique du Probléme Restreint: I, Masses Eagles, Orbites Périodiques. Annales D' Astrophysque. 1965;28:499–512.
[26] Hénon M. Exploration Numérique du Probléme restreint: II, masses eagles, Stabilité des orbites Périodiques. Annales D' Astrophysque. 1965;28:992–1007.
[27] Hénon M. Families of asymmetric periodic orbits in Hill's problem of three bodies. Cel Mech Dyn Astr. 2005;93:87–100.
[28] Markellos VV, Halioulias AA. Numerical determination of asymmetric periodic solutions. Astrophys Space Sci. 1977;46:183–93.